

# A 25 THz bandwidth THz spectroscopy system exploiting BNA crystals and a tunable single-ring-fiber pulse compressor

WEI CUI,<sup>1,\*</sup> ASWIN VISHNURADHAN,<sup>1</sup> MARKUS LIPPL,<sup>2,3</sup> EESWAR KUMAR YALAVARTHI,<sup>1</sup> ANGELA GAMOURAS,<sup>1,4</sup> NICOLAS Y. JOLY,<sup>2,3,5</sup> AND JEAN-MICHEL MÉNARD<sup>1,4,\*</sup>

<sup>1</sup> University of Ottawa, Department of Physics, 25 Templeton Street, Ottawa, Ontario K1N 6N5, Canada

<sup>2</sup> Max Planck Institute for the Science of Light, Staudtstr. 2, 91058 Erlangen, Germany

<sup>3</sup> Department of Physics, University of Erlangen-Nürnberg, Staudtstr. 2, 91058 Erlangen, Germany

<sup>4</sup> National Research Council Canada, 1200 Montreal Road, Ottawa, Ontario K1A 0R6, Canada

<sup>5</sup> Integrated center for nanostructured films, Cauerstr. 3, 91058 Erlangen

\*wcui065@uottawa.ca; jean-michel.menard@uOttawa.ca

**Abstract:** We present a terahertz time-domain spectroscopy (THz-TDS) system which accesses a broadband spectrum, efficiently covering the so-called “new THz gap” between 5 and 15 THz and extending beyond 25 THz. The system exploits nonlinear interactions within the organic crystal BNA (N-benzyl-2-methyl-4-nitroaniline) to generate and detect THz radiation upon excitation by a near-infrared (NIR) pulse centered at 1.03 μm. To enable broadband THz spectral monitoring, the NIR pulse from a Yb-based solid-state laser undergoes spectral broadening in a gas-filled single-ring hollow-core photonic crystal fiber, followed by a pulse compression to achieve durations as short as 31 fs. This approach paves the way for broadband spectroscopy in hard-to-access THz regions using widely available near-infrared ultrafast sources.

## 1. Introduction

Terahertz time-domain spectroscopy (THz-TDS) is a non-invasive technique capable of phase-sensitive measurements, allowing direct access to the complex dielectric properties of materials<sup>1</sup>. The technique has found widespread use in scientific research to monitor a vast range of fundamental excitations in fascinating solid-state systems such as superconductors<sup>2–4</sup>, topological insulators<sup>5,6</sup>, Dirac and Weyl semimetals<sup>7,8</sup>, heavy fermion systems<sup>9,10</sup>, and quantum spin liquids<sup>11,12</sup>. Furthermore, due to its capacity to distinguish unique spectral signatures of organic and inorganic materials, the technique holds significant potential for industrial quality monitoring. Expanding the operational bandwidth of THz-TDS is essential for accessing more information as it not only advances our understanding of the underlying physics in emerging materials but also enables new applications in sensing and imaging<sup>13–15</sup>.

The development of broadband THz-TDS systems has been in part limited by the availability of nonlinear devices allowing efficient THz generation and detection at frequencies between 5 and 15 THz<sup>16,17</sup>. Photoconductive methods for THz emission and detection are extensively employed because of their straightforward design and compact structure. However, phonon absorption and electronic dynamics usually prevent these devices to efficiently reach frequencies above 10 THz<sup>18</sup>. Other systems using optical rectification (OR) for THz generation and electro-optic sampling (EOS) for detection, rely on noncentrosymmetric materials featuring a strong second-order ( $\chi^{(2)}$ ) nonlinearity, favorable phase-matching conditions, and low absorption in both the NIR and THz spectral windows. Finding a material with a relatively low absorption over a large THz window is particularly difficult to satisfy, as most materials exhibit

strong absorption between 5 and 15 THz due to optical phonons<sup>16,17</sup>. One way to circumvent these material limitations is by using two-color laser-induced plasma generation in gas<sup>15,19</sup>, which must be combined with air-based coherent detection<sup>20</sup>. This scheme, however, requires a mJ-pulse-energy laser source and a relatively complex optical configuration. Spintronic emitters have also emerged as capable sources to generate broadband THz radiation without being limited by phase-matching constraints<sup>21</sup>. However, their optical-to-terahertz conversion efficiency has remained so far lower than many optical rectification techniques<sup>22</sup>. As another alternative, broadband THz pulses can be generated with Raman-resonance-enhanced four-wave mixing in diamond. However, this technique requires tightly synchronized multi-pulse excitation, precise angular alignment for phase matching, and high peak intensities, making it experimentally more complex than conventional methods<sup>23</sup>.

The emergence of organic crystals offers new possibilities for THz-TDS. They feature a high  $\chi^{(2)}$  nonlinearity, satisfaction of phase-matching conditions at common NIR laser wavelengths and low THz absorption due to their weaker phonon resonances than semiconductors. Most organic materials studied to date, such as DAST, DSTMS, and OH1, satisfy phase-matching conditions near 1550 nm<sup>24</sup>. BNA (N-benzyl-2-methyl-4-nitroaniline) crystals have been shown to efficiently generate THz radiation up to 5 THz when driven by ultrashort pulses centered at 800 nm<sup>25-27</sup>. At an excitation wavelength of 1030 nm, BNA emerges as a particularly promising material for broadband spectroscopy, enabling THz generation over a wider bandwidth while exhibiting comparatively weak resonant absorption<sup>28-30</sup>. Previous work demonstrated the potential of BNA pumped at 1030 nm to generate broadband, high-field THz pulses, including a record electric field strength of 1 MV/cm<sup>31</sup>, as well as record-high average THz output powers reaching 5.6 mW<sup>28,32,33</sup>. However, the accessible THz bandwidth of these systems remain limited by the nonlinear detection technique relying on semiconductor crystals, such as GaP. A potential solution is to also use organic crystals as electro-optic crystal to achieve broadband THz detection<sup>34-37</sup>. However, such experiments remain challenging, primarily due to the strong birefringence of these crystals, which complicate polarization-sensitive THz detection techniques. Among recent approaches, THz-induced lensing (TIL)-based electro-optic sampling has been shown to mitigate birefringence-related challenges in strongly anisotropic organic crystals, although it requires alignment-sensitive detection optics<sup>34,36</sup>. Schneider *et al.* first demonstrated a fully organic THz system using DAST crystals for both THz generation and TIL-based detection<sup>34</sup>. Later, Puc *et al.* employed DAST and DSTMS under 1560 nm excitation, also using TIL detection to obtain nearly 25 THz of detectable bandwidth<sup>36</sup>. In contrast, Kuroyanagi *et al.* showed that conventional polarization-based EOS can be implemented using BNA for both generation and detection at 815 nm, achieving a bandwidth of 8 THz<sup>35</sup>. Most recently, Mansourzadeh *et al.* demonstrated THz generation and conventional EOS detection with MNA, reaching an ~9 THz bandwidth<sup>37</sup>. Collectively, these works illustrate both the promise and the limitations of organic-crystal THz systems, particularly in scaling the detection bandwidth while maintaining high sensitivity at elevated THz frequencies.

Another significant challenge in developing broadband THz-TDS systems is the need for a high-cost ultrafast optical source with a sufficiently short pulse duration and broad spectral bandwidth to enable THz generation and detection at high frequencies. For example, most systems based on commercially available Yb:KGW NIR sources delivering >100 fs pulses centered at 1030 nm typically offer bandwidths of 4 THz or less. To extend the accessible THz window beyond this limit, pulse compressing methods such as multi-pass cell<sup>38</sup>, gas-filled hollow-core fibers (HCFs)<sup>39</sup> or gas-filled hollow-core photonic crystal fibers (HC-PCFs) have been demonstrated<sup>40</sup>. Spectrally broadened 1030 nm lasers generated using these techniques have been applied to efficiently produce broadband THz radiation in organic crystals<sup>28,31,37,41</sup>. The main advantage of the HC-PCFs is the ability to control linear dispersion and nonlinearity by adjusting the gas pressure and gas composition within the hollow core. This approach has

been successfully demonstrated using an argon-filled kagomé HC-PCF<sup>42</sup>, doubling the bandwidth of a THz-TDS system based on GaP crystals for THz generation and detection. Replacing GaP with GaSe further extends the accessible THz spectral range, enabling tunable multi-THz emission between 10 and 18 THz<sup>43</sup>. Recently developed single-ring HC-PCFs retain the key advantages of kagomé HC-PCFs, such as pressure-tunable dispersion and nonlinearity, while avoiding the unpredictable loss bands due to the complex structure and can therefore offer lower loss while being easier to fabricate<sup>44,45</sup>.

In this manuscript, we present an ultra-broadband THz-TDS system relying on BNA crystals, for both THz generation and detection, while taking advantage of a single-ring HC-PCFs to compress the NIR pulses produced by a commercial Yb:KGW ultrafast amplifier. This configuration is timely, since this type of lasers is increasingly likely to gain broader adoption than Ti:sapphire systems across a range of ultrafast applications<sup>46</sup>. Combining these approaches, we demonstrate a THz-TDS to access a frequency range extending from 0.3 to 25.2 THz, with a significant portion of the generated spectrum covering the “new THz gap” between 5 and 15 THz. This spectral coverage establishes a powerful platform for exploring phonons and polaritons in two-dimensional and semiconductor systems<sup>47-49</sup>, as well as emergent excitations in quantum materials<sup>50</sup>. Our configuration has the potential to extend the accessible spectral range beyond that previously achieved with Yb-based organic-crystal systems, offering a broadband and streamlined single-color THz-TDS approach.

## 2. Experiments

Figure 1 shows a schematic of the experimental apparatus. A single-ring HC-PCF is placed before a standard THz-TDS configuration relying on organic BNA crystals for THz generation and detection<sup>42</sup>. The system is driven by a commercial Yb:KGW regenerative amplifier system generating 180 fs pulses centered at 1035 nm and operating at a repetition rate of 1.1 MHz. The NIR pulses are launched into a single-ring HC-PCF with an 85% coupling efficiency. The scanning electron micrograph of the transverse structure of the single-ring HC-PCF is shown in the inset of Fig. 1. The HC-PCF is 55 cm long, with a core diameter  $D \sim 37 \mu\text{m}$ , a hollow capillary diameter  $d \sim 28 \mu\text{m}$  and a capillary wall thickness of 300 nm. The HC-PCF is enclosed in a gas cell filled with argon gas at 15 bar, which serves as nonlinear medium for spectral broadening. At this pressure the fiber exhibits anomalous dispersion over the used spectral range (zero dispersion lies at 850 nm), therefore the fiber length had to be chosen such that one can only observe self-phase modulation (SPM) and no soliton fission can occur. The length scale for soliton fission to take place is estimated to be 75 cm<sup>51</sup> at the highest energy available at the given laser repetition rate (considering the coupling efficiency), in order to have sufficient safety margin a fiber length of 55 cm was chosen. This limitation means that the negative dispersion of the fiber is not sufficient to yield a transform-limited pulse. To compensate for the remaining positive chirp a pair of chirped mirrors providing a dispersion of  $-250 \text{ fs}^2$  per reflection is placed after the fiber output. The number of chirped-mirror bounces applied to the NIR pulse after the single-ring fiber is determined by continuously varying the number of bounces from 3 to 16 and using intensity autocorrelation measurements to identify the shortest pulse duration. The beam is then guided into a THz-TDS system<sup>42</sup>. In such a system, the beam is split into two arms by a beam splitter (BS). The transmitted beam is focused onto a 400  $\mu\text{m}$ -thick BNA crystal attached to a 500  $\mu\text{m}$ -thick z-cut sapphire to generate THz through optical rectification. The NIR generation pulse incident on the generation crystal has a spot size of 24.8  $\mu\text{m}$  ( $1/e^2$  diameter). The excitation beam is attenuated to a pulse energy below 0.15  $\mu\text{J}$  to prevent damaging the BNA crystal. Another beam, reflected by the BS, is used for THz detection using the EOS technique. The

EOS crystal is a free-standing 400  $\mu\text{m}$ -thick BNA crystal. The NIR gating pulse incident on the detection crystal has a spot size of 8.2  $\mu\text{m}$  ( $1/e^2$  diameter). A motorized linear translation stage was used to sample the terahertz waveform point by point with a step size of  $\Delta x = 1.5 \mu\text{m}$ , corresponding to a temporal increment of  $\Delta t = 10 \text{ fs}$ . A lock-in amplifier with a time constant of 100 ms and an additional waiting time of 500 ms at each step enabled sensitive acquisition of 500 temporal points within approximately 8 min. The waiting time dramatically limits the acquisition speed but is especially important here, since the stop-and-go motion of the translation stage induces beam-pointing instabilities. Coupled with inhomogeneities in the detection crystal, this requires a long settling time to ensure reliable measurements. Techniques demonstrated in the literature could be implemented to address this issue, notably asynchronous optical sampling (ASOPS)<sup>52</sup> based on two synchronized ultrafast lasers, as well as other fast-scanning approaches<sup>53,54</sup>.

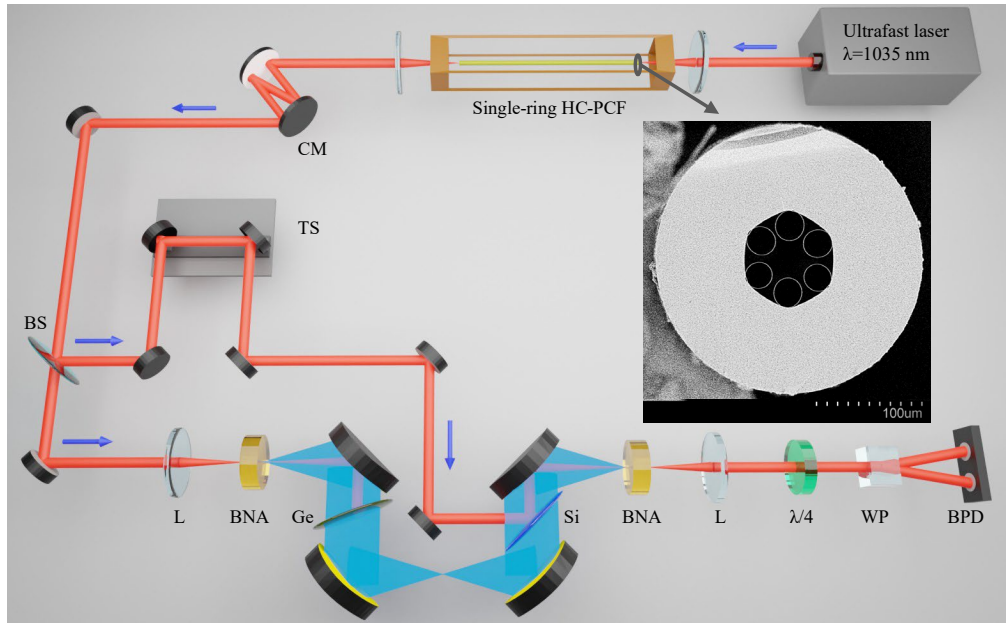


Fig. 1. Schematic of the experimental setup. NIR pulses from the ultrafast laser are launched into a single-ring HC-PCF filled with argon gas at 15 bar. A standard THz-TDS system<sup>1,42</sup> is then used to generate and detect THz pulses. The system operates in a dry-air purged environment. CM: chirped mirror; BS: beam splitter; TS: translational stage; L: lens; BNA: N-benzyl-2-methyl-4-nitroaniline generation/detection crystal; Ge: Germanium wafer; Si: Silicon wafer;  $\lambda/4$ : quarter-wave plate; WP: Wollaston prism; BPD: balanced photodetectors.

### 3. Results and discussion

The NIR spectra after the HC-PCF and CMs is shown as a function of the input pulse energy  $E_p$  in Fig. 2(a). At  $E_p = 0.92 \mu\text{J}$ , the spectrum reaches a spectral bandwidth of 7.7 THz full-width at half-maximum (FWHM). As the launched NIR pulse energy is increased up to 4.16  $\mu\text{J}$ , the bandwidth also gradually increases up to 32 THz (FWHM). At  $E_p \geq 1.39 \mu\text{J}$ , concentration of optical energy is observed within spectral lobes at the edges of the spectrum. This uneven energy distribution enables more efficient THz generation at frequencies corresponding to the spectral separation of these lobes<sup>43</sup>. The second-harmonic autocorrelation traces obtained with a 30- $\mu\text{m}$ -thick beta-barium borate (BBO) crystal are shown in Fig. 2(b). For an input pulse energy of 0.92  $\mu\text{J}$  and after 6 bounces off the CMs, the pulse duration obtained after deconvolution is measured to be 106 fs FWHM, assuming a Gaussian pulse

shape. As the input pulse energy increases up to  $2.77 \mu\text{J}$ , the pulse duration decreases, reaching a minimum of 31 fs. At higher input pulse energies, spectral broadening extends beyond the operational bandwidth of the CMs, which requires us to use 4 bounces to achieve the minimum pulse duration. As the generated spectrum increases with increasing input pulse energy the pulse acquires more negative chirp. This is why at higher pulse energies we were only required to use 4 bounces to achieve the minimum pulse duration. We measure a pulse duration of 40 fs at  $E_p = 3.23 \mu\text{J}$ , 34 fs at  $E_p = 3.70 \mu\text{J}$  and 32 fs at  $E_p = 4.16 \mu\text{J}$  using the same configuration. The structured pedestals may also arise from higher-order dispersion components that cannot be compensated by the chirped mirrors used in this work.

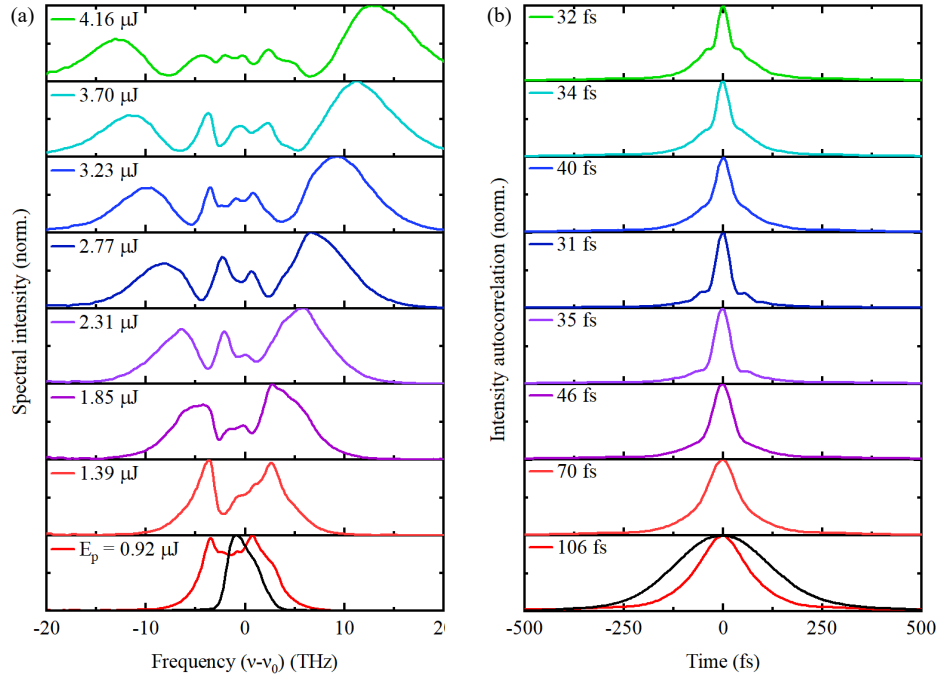


Fig. 2. (a) Measured NIR spectra after the single-ring HC-PCF with different input pulse energies  $E_p$ . (b) Measured intensity autocorrelation traces of the NIR pulses shown in (a) after reflecting off a pair of CMs. The FWHM of the original NIR pulse obtained after deconvolution (assuming a Gaussian pulse shape) is shown in the top-left corner. For  $E_p$  going up to  $2.77 \mu\text{J}$ , the NIR pulses exiting the fiber experience six bounces on the CMs, while only four bounces on the CMs are used before collecting measurements at higher  $E_p$ . Black lines in the bottom panels of (a) and (b) show the laser spectrum and autocorrelation trace of the laser featuring a 3.5 THz spectral width (FWHM) and 185 fs pulse duration.

To evaluate the effectiveness of the BNA crystal for nonlinear THz detection, we compare the THz signals measured by electro-optic sampling with a 300  $\mu\text{m}$ -thick free-standing BNA crystal and a reference 300  $\mu\text{m}$ -thick GaP crystal. For these measurements,  $E_p$  is set to  $2.31 \mu\text{J}$ , corresponding to a pulse duration of 35 fs. Broadband THz pulses centered around 2.6 THz are generated by tilted-pulse-front phase matching inside a 1-mm-thick GaP crystal, enabled by a phase grating etched directly onto the front surface of the crystal<sup>55,56</sup>. We monitor the THz temporal waveform and corresponding spectral amplitude obtained by the Fourier transform (Fig. 3). In the time domain, the peak signal detected with BNA reaches only 15% of that

obtained with GaP, despite BNA exhibiting a larger second-order nonlinear coefficient<sup>24</sup>. Notably, substantial variations in signal amplitude are observed when the position of the gating pulse is shifted across the 300  $\mu\text{m}$ -thick BNA crystal. This reduction in EOS signal is attributed to BNA's intrinsic birefringence and spatial inhomogeneity, which induce decoherence during gating pulse propagation. Frequency-domain analysis reveals that both 300  $\mu\text{m}$ -thick BNA and GaP crystals are suitable to detect frequencies up to 6 THz. However, BNA demonstrates a distinct advantage in resolving higher-frequency components. The spectral response of BNA also exhibits phonon resonances at 2.2 and 3.3 THz, consistent with previous reports<sup>32,57</sup>.

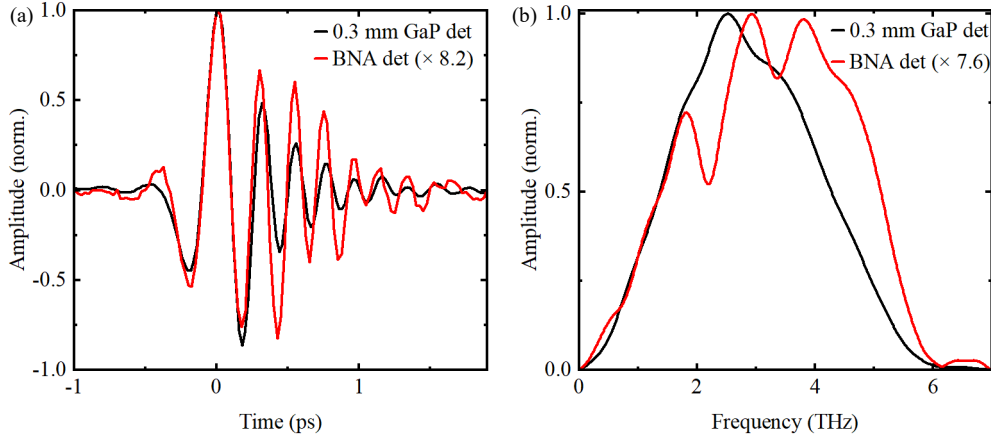


Fig. 3. (a) THz transients and (b) spectral amplitudes measured using a 300- $\mu\text{m}$ -thick GaP (black) and a 400  $\mu\text{m}$ -thick free-standing BNA (red) at  $E_p = 2.31 \mu\text{J}$ . The generation crystal is 1-mm-thick GaP crystal with a grating etched on the front surface<sup>55,56</sup>. In both plots, the THz waveforms and spectra are normalized to their own maximum values.

The highest frequency component that can be resolved, around 6.5 THz, is in fact limited by the THz emission process. To access a larger THz spectral window, we replace the THz generation crystal with a 400- $\mu\text{m}$ -thick BNA crystal. Figure 4 shows the THz temporal waveforms and corresponding spectral amplitudes measured as we vary the input pulse energies  $E_p$  in the HC-PCF-based pulse compressor. Increasing  $E_p$  spectrally broadens and temporally compresses NIR pulses allowing access to a larger THz spectral window through broadband optical rectification and EOS sampling. At  $E_p = 0.92 \mu\text{J}$ , the THz time-domain signal appears as a multi-cycle pulse spanning over 2 ps. The corresponding spectrum extends up to 10.3 THz with most of the energy concentrated between 2.5 and 7.5 THz. At  $E_p = 1.39 \mu\text{J}$ , the time-domain signal exhibits higher frequency oscillations and a spectral component emerging at 11 THz. As we increase  $E_p$  to 2.77  $\mu\text{J}$ , the THz spectrum efficiently covers low frequencies as well as the region between 7.5-12.5 THz. At  $E_p = 3.23 \mu\text{J}$ , new spectral components appear near 13.5 THz and 20.5 THz. Finally, at  $E_p \geq 3.23 \mu\text{J}$ , additional THz components emerge between 17 and 25 THz. In the time domain, the maximum THz electric field measured at a pump pulse energy of  $E_p = 3.70 \mu\text{J}$  is approximately five times larger than that measured at  $E_p = 0.92 \mu\text{J}$ . In the spectral domain, the maximum spectral amplitude at  $E_p = 4.16 \mu\text{J}$  is approximately seven times larger than that at  $E_p = 0.92 \mu\text{J}$ , with the spectral peaks located at 10.8 THz and 5.3 THz, respectively. In this work, only a single detection-crystal thickness was investigated. A systematic study of crystals with different thicknesses would be essential to determine the optimal conditions for THz emission and detection. Future work should therefore combine experimental studies across varying thicknesses with simulations, once reliable high-frequency optical constants of BNA become available. Furthermore, because the present system

provides broadband access across and beyond the “new THz gap”, it offers a promising route to experimentally determine the high-frequency optical constants of BNA and other organic crystals, providing the data needed for future optimization studies.

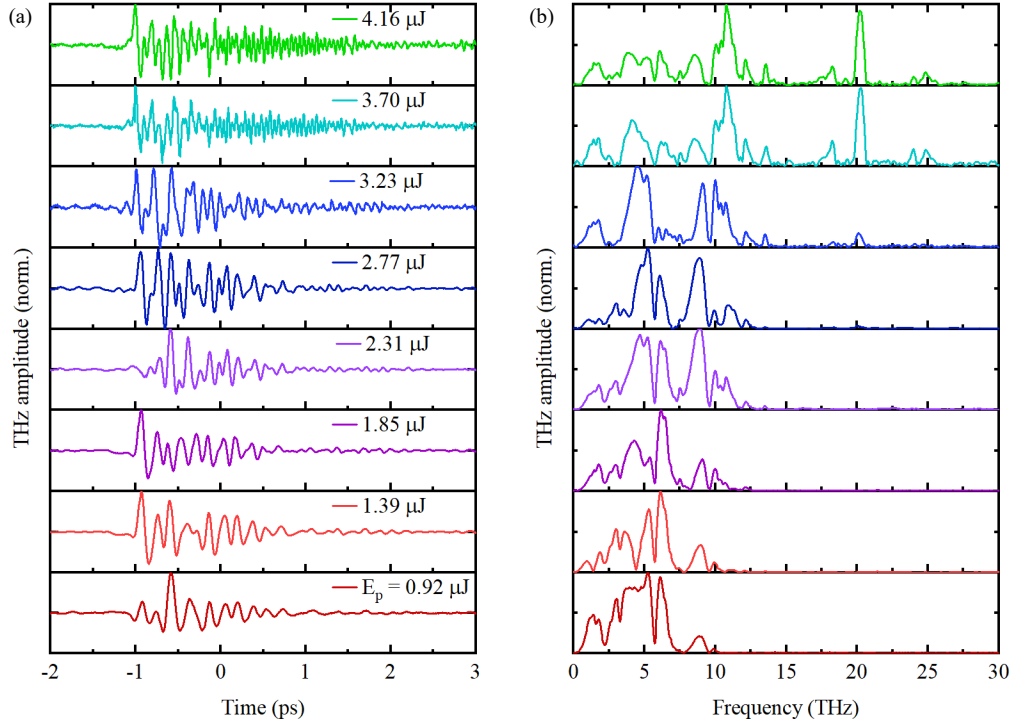


Fig. 4. (a) Measured THz time-domain signal and (b) spectral amplitude obtained with  $E_p$  ranging from 0.92 to 4.16  $\mu\text{J}$ . As  $E_p$  increases, the time-domain signals display progressively faster oscillations, reflected in the appearance of higher-frequency components in the spectral domain.

We evaluate the sensitivity of our broadband THz-TDS system by characterizing the THz spectral intensity and noise floor at  $E_p = 4.16 \mu\text{J}$ . The result shown in Fig. 5 corresponds to a single scan, acquired over 8 minutes to cover a 5 ps range with 10 fs resolution. The spectral noise floor, acquired under identical conditions with the THz beam blocked, is fitted to the model  $A(1/f + B)$ , which accounts for 1/f pink noise, where  $f$  is the frequency and  $A$  and  $B$  are fitting parameters<sup>1,55</sup>. We observe a broad signal covering the window between 0.7 and 25.2 THz and featuring a maximum dynamic range (DR) of 55 dB at 11 THz. Notably, we find a DR generally approaching three orders of magnitude in the hard-to-access region between 3 and 13 THz. Although some phonon absorption dips are present, the DR remains robust, only exhibiting a pronounced decline below 1000, only reaching a minimum of  $\sim 100$  near 9.5 THz. Previous experiments relying on two-beam difference-frequency generation in BNA<sup>29,30</sup> also demonstrated access to a similar spectral bandwidth. However, the generated spectrum with such a scheme is relatively narrowband and requires tunable, dual-wavelength NIR source to

access the full spectral range. Here, our approach combining a Yb:KGW laser source and a single-ring HC-PCF provides access to a broadband THz region in a single measurement.

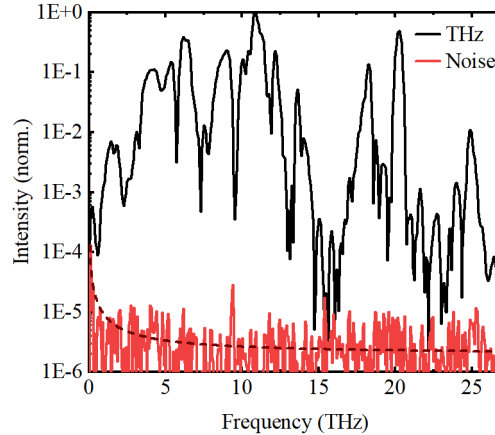


Fig. 5. THz spectral intensity (black curve) and noise floor (red curve). The dashed line is the noise floor fitted to the model  $A(1/f+B)$ , where  $f$  is the frequency, while  $A$  and  $B$  are fitting parameters<sup>1,55</sup>.

#### 4. Conclusion

We present a THz-TDS system that uses a gas-filled single-ring HC-PCF to compress NIR pulses centered at  $1.03\text{ }\mu\text{m}$ , enabling the generation and detection of broadband THz transients in BNA crystals. This approach provides access to a frequency window between  $0.3\text{ THz}$  and  $25.2\text{ THz}$ , unlocking new possibilities for spectroscopy applications. Interestingly, a significant portion of the generated THz energy falls between  $3$  and  $13\text{ THz}$ , effectively addressing the “new THz gap,” which has been challenging to access with conventional THz-TDS configurations. Additionally, our system leverages flourishing Yb:KGW laser technology, offering compact and cost-effective alternative to configurations relying on a dual-wavelength excitation for THz generation. Our results demonstrate a promising platform for sensitive, broadband THz spectroscopy, with potential applications in ultrafast carrier dynamics, vibrational spectroscopy of complex materials, and emerging fields such as chemical sensing, biomedical diagnostics, and high-speed optoelectronics.

#### Acknowledgments

J.-M.M. acknowledges funding from the Natural Sciences and Engineering Research Council of Canada (Grant No. RGPIN-2023-05365) and the Canada Foundation for Innovation (Project No. 35269). This work is also supported by the National Research Council of Canada via the High Throughput and Secure Networks Challenge Program (HTSN 254) and the Joint Centre for Extreme Photonics.

#### Disclosures

The authors declare that there are no conflicts of interest related to this article.

## References

- <sup>1</sup> J. Neu, and C.A. Schmuttenmaer, "Tutorial: An introduction to terahertz time domain spectroscopy (THz-TDS)," *Journal of Applied Physics* **124**(23), 231101 (2018).
- <sup>2</sup> R. Matsunaga, Y.I. Hamada, K. Makise, Y. Uzawa, H. Terai, Z. Wang, and R. Shimano, "Higgs Amplitude Mode in the BCS Superconductors  $Nb_{1-x}Ti_xN$  Induced by Terahertz Pulse Excitation," *Phys. Rev. Lett.* **111**(5), 057002 (2013).
- <sup>3</sup> B. Cheng, D. Cheng, K. Lee, L. Luo, Z. Chen, Y. Lee, B.Y. Wang, M. Mootz, I.E. Perakis, Z.-X. Shen, H.Y. Hwang, and J. Wang, "Evidence for d-wave superconductivity of infinite-layer nickelates from low-energy electrodynamics," *Nature Materials* **23**(6), 775–781 (2024).
- <sup>4</sup> J.E. Lee, J. Choi, T.S. Jung, J.H. Kim, Y.J. Choi, K.I. Sim, Y. Jo, and J.H. Kim, "Gapless superconductivity in Nb thin films probed by terahertz spectroscopy," *Nature Communications* **14**(1), 2737 (2023).
- <sup>5</sup> L. Wu, M. Brahlek, R. Valdés Aguilar, A.V. Stier, C.M. Morris, Y. Lubashevsky, L.S. Bilbro, N. Bansal, S. Oh, and N.P. Armitage, "A sudden collapse in the transport lifetime across the topological phase transition in  $(Bi_{1-x}In_x)_2Se_3$ ," *Nature Phys* **9**(7), 410–414 (2013).
- <sup>6</sup> B.C. Park, T.-H. Kim, K.I. Sim, B. Kang, J.W. Kim, B. Cho, K.-H. Jeong, M.-H. Cho, and J.H. Kim, "Terahertz single conductance quantum and topological phase transitions in topological insulator  $Bi_2Se_3$  ultrathin films," *Nature Communications* **6**(1), 6552 (2015).
- <sup>7</sup> B. Cheng, T. Schumann, S. Stemmer, and N.P. Armitage, "Probing charge pumping and relaxation of the chiral anomaly in a Dirac semimetal," *Science Advances* **7**(16), eabg0914 (2021).
- <sup>8</sup> B. Cheng, Y. Wang, D. Barbalas, T. Higo, S. Nakatsuji, and N.P. Armitage, "Terahertz conductivity of the magnetic Weyl semimetal  $Mn_3Sn$  films," *Appl. Phys. Lett.* **115**(1), 012405 (2019).
- <sup>9</sup> G. Bossé, L. Pan, Y.S. Li, L.H. Greene, J. Eckstein, and N.P. Armitage, "Anomalous frequency and temperature-dependent scattering and Hund's coupling in the almost quantum critical heavy-fermion system  $CeFe_2Ge_2$ ," *Phys. Rev. B* **93**(8), 085104 (2016).
- <sup>10</sup> L. Prochaska, X. Li, D.C. MacFarland, A.M. Andrews, M. Bonta, E.F. Bianco, S. Yazdi, W. Schrenk, H. Detz, A. Limbeck, Q. Si, E. Ringe, G. Strasser, J. Kono, and S. Paschen, "Singular charge fluctuations at a magnetic quantum critical point," *Science* **367**(6475), 285–288 (2020).
- <sup>11</sup> P. Chauhan, F. Mahmood, H.J. Changlani, S.M. Koohpayeh, and N.P. Armitage, "Tunable Magnon Interactions in a Ferromagnetic Spin-1 Chain," *Phys. Rev. Lett.* **124**(3), 037203 (2020).
- <sup>12</sup> Z. Wang, S. Reschke, D. Hüvonen, S.-H. Do, K.-Y. Choi, M. Gensch, U. Nagel, T. Rööm, and A. Loidl, "Magnetic Excitations and Continuum of a Possibly Field-Induced Quantum Spin Liquid in  $\alpha$ -RuCl<sub>3</sub>," *Phys. Rev. Lett.* **119**(22), 227202 (2017).
- <sup>13</sup> C. Riek, D.V. Seletskiy, A.S. Moskalenko, J.F. Schmidt, P. Krauspe, S. Eckart, S. Eggert, and A. Leitenstorfer, "Direct sampling of electric-field vacuum fluctuations," *Science* **350**, 420 (2015).
- <sup>14</sup> T. Siday, F. Sandner, S. Brem, M. Zizlsperger, R. Perea-Causin, F. Schiegl, S. Netteer, M. Plankl, P. Merkl, F. Mooshamer, M.A. Huber, E. Malic, and R. Huber, "Ultrafast Nanoscopy of High-Density Exciton Phases in WSe<sub>2</sub>," *Nano Lett.* **22**(6), 2561–2568 (2022).
- <sup>15</sup> A.T. Tarekegne, B. Zhou, K. Kaltenegger, K. Iwaszcuk, S. Clark, and P.U. Jepsen, "Terahertz time-domain spectroscopy of zone-folded acoustic phonons in 4H and 6H silicon carbide," *Opt. Express*, **OE** **27**(3), 3618–3628 (2019).
- <sup>16</sup> S.S. Dhillon, M.S. Vitiello, E.H. Linfield, A.G. Davies, M.C. Hoffmann, J. Booske, C. Paoloni, M. Gensch, P. Weightman, G.P. Williams, E. Castro-Camus, D.R.S. Cumming, F. Simoens, I. Escoria-Carranza, J. Grant, S. Lucyszyn, M. Kuwata-Gonokami, K. Konishi, M. Koch, C.A. Schmuttenmaer, T.L. Cocker, R. Huber, A.G. Markelz, Z.D. Taylor, V.P. Wallace, J. Axel Zeitler, J. Sibik, T.M. Korter, B. Ellison, S. Rea, P. Goldsmith, K.B. Cooper, R. Appleby, D. Pardo, P.G. Huggard, V. Krozer, H. Shams, M. Fice, C. Renaud, A. Seeds, A. Stöhr, M. Naftaly, N. Ridler, R. Clarke, J.E. Cunningham, and M.B. Johnston, "The 2017 terahertz science and technology roadmap," *J. Phys. D: Appl. Phys.* **50**(4), 043001 (2017).
- <sup>17</sup> A. Leitenstorfer, A.S. Moskalenko, T. Kampfrath, J. Kono, E. Castro-Camus, K. Peng, N. Qureshi, D. Turchinovich, K. Tanaka, A.G. Markelz, M. Havenith, C. Hough, H.J. Joyce, W.J. Padilla, B. Zhou, K.-Y. Kim, X.-C. Zhang, P.U. Jepsen, S. Dhillon, M. Vitiello, E. Linfield, A.G. Davies, M.C. Hoffmann, R. Lewis, M. Tonouchi, P. Klarskov, T.S. Seifert, Y.A. Gerasimenko, D. Mihailovic, R. Huber, J.L. Boland, O. Mitrofanov, P. Dean, B.N. Ellison, P.G. Huggard, S.P. Rea, C. Walker, D.T. Leisawitz, J.R. Gao, C. Li, Q. Chen, G. Valušis, V.P. Wallace, E. Pickwell-MacPherson, X. Shang, J. Hesler, N. Ridler, C.C. Renaud, I. Kallfass, T. Nagatsuma, J.A. Zeitler, D. Arnone, M.B. Johnston, and J. Cunningham, "The 2023 terahertz science and technology roadmap," *J. Phys. D: Appl. Phys.* **56**(22), 223001 (2023).
- <sup>18</sup> R.B. Kohlhaas, S. Breuer, S. Mutschall, M. Kehrt, S. Nellen, L. Liebermeister, M. Schell, and B. Globisch, "Ultrabroadband terahertz time-domain spectroscopy using III-V photoconductive membranes on silicon," *Opt. Express* **30**(13), 23896–23908 (2022).
- <sup>19</sup> E. Matsubara, M. Nagai, and M. Ashida, "Ultrabroadband coherent electric field from far infrared to 200 THz using air plasma induced by 10 fs pulses," *Appl. Phys. Lett.* **101**(1), 011105 (2012).
- <sup>20</sup> J. Dai, X. Xie, and X.-C. Zhang, "Detection of Broadband Terahertz Waves with a Laser-Induced Plasma in Gases," *Phys. Rev. Lett.* **97**(10), 103903 (2006).

<sup>21</sup> T.S. Seifert, L. Cheng, Z. Wei, T. Kampfrath, and J. Qi, “Spintronic sources of ultrashort terahertz electromagnetic pulses,” *Appl. Phys. Lett.* **120**(18), 180401 (2022).

<sup>22</sup> P. Koleják, G. Lezier, D. Vala, B. Mathmann, L. Halagáčka, Z. Gelnárová, Y. Dusch, J.-F. Lampin, N. Tiercelin, K. Postava, and M. Vanwolleghem, “Maximizing the Electromagnetic Efficiency of Spintronic Terahertz Emitters,” *Advanced Photonics Research* **5**(11), 2400064 (2024).

<sup>23</sup> J. Le, Y. Su, C. Tian, A.H. Kung, and Y.R. Shen, “A novel scheme for ultrashort terahertz pulse generation over a gapless wide spectral range: Raman-resonance-enhanced four-wave mixing,” *Light Sci Appl* **12**(1), 34 (2023).

<sup>24</sup> S. Mansourzadeh, T. Vogel, A. Omar, T.O. Buchmann, E.J.R. Kelleher, P.U. Jepsen, and C.J. Saraceno, “Towards intense ultra-broadband high repetition rate terahertz sources based on organic crystals [Invited],” *Opt. Mater. Express*, **OME** **13**(11), 3287–3308 (2023).

<sup>25</sup> M. Shalaby, C. Vicario, K. Thirupugalmani, S. Brahadeeswaran, and C.P. Hauri, “Intense THz source based on BNA organic crystal pumped at Ti:sapphire wavelength,” *Opt. Lett.*, **OL** **41**(8), 1777–1780 (2016).

<sup>26</sup> Z.B. Zaccardi, I.C. Tangen, G.A. Valdivia-Berroeta, C.B. Bahr, K.C. Kenney, C. Rader, M.J. Lutz, B.P. Hunter, D.J. Michaelis, and J.A. Johnson, “Enabling high-power, broadband THz generation with 800-nm pump wavelength,” *Opt. Express* **29**(23), 38084 (2021).

<sup>27</sup> H. Chen, G.-Q. Liao, H.-Y. Wu, H.-Y. Lei, J.-Y. Ruan, Y.-Y. Wei, Y.-F. Li, J.-G. Wang, F.-Z. Sun, X. Wang, X. Lu, and Y.-T. Li, “Optimized terahertz generation in BNA organic crystals with chirped Ti:sapphire laser pulses,” *Opt. Lett.*, **OL** **49**(18), 5047–5050 (2024).

<sup>28</sup> Y.-G. Jeong, L. Zanotto, D.-J. Seo, Y. Nam, X. Jin, J. Kyoung, B.E. Schmidt, M. Shalaby, and L. Razzari, “Multi-microjoule broadband terahertz generation in the organic crystal BNA pumped by ytterbium laser pulses compressed via a gas-filled hollow-core fiber,” *Opt. Lett.*, **OL** **50**(2), 530–533 (2025).

<sup>29</sup> K. Miyamoto, S. Ohno, M. Fujiwara, H. Minamide, H. Hashimoto, and H. Ito, “Optimized terahertz-wave generation using BNA-DFG,” *Opt. Express* **17**(17), 14832 (2009).

<sup>30</sup> T. Notake, K. Nawata, H. Kawamata, T. Matsukawa, F. Qi, and H. Minamide, “Development of an ultra-widely tunable DFG-THz source with switching between organic nonlinear crystals pumped with a dual-wavelength BBO optical parametric oscillator,” *Opt. Express* **20**(23), 25850 (2012).

<sup>31</sup> K. Brekhov, S. Colar, E. Chiglintsev, and A. Chernov, “Efficient strong-field THz generation from BNA organic crystal pumped by a 1030 nm Yb-laser,” *Opt. Express* **33**(14), 30505–30514 (2025).

<sup>32</sup> S. Mansourzadeh, T. Vogel, A. Omar, M. Shalaby, M. Cinchetti, and C.J. Saraceno, “Broadband, high power THz source at 540 kHz using organic crystal BNA,” *APL Photonics* **8**(1), 011301 (2023).

<sup>33</sup> S. Mansourzadeh, T. Vogel, M. Shalaby, F. Wulf, and C.J. Saraceno, “Milliwatt average power, MHz-repetition rate, broadband THz generation in organic crystal BNA with diamond substrate,” *Opt. Express*, **OE** **29**(24), 38946–38957 (2021).

<sup>34</sup> A. Schneider, I. Biaggio, and P. Günter, “Terahertz-induced lensing and its use for the detection of terahertz pulses in a birefringent crystal,” *Applied Physics Letters* **84**(13), 2229–2231 (2004).

<sup>35</sup> K. Kuroyanagi, M. Fujiwara, H. Hashimoto, H. Takahashi, S. Aoshima, and Y. Tsuchiya, “All Organic Terahertz Electromagnetic Wave Emission and Detection Using Highly Purified N-Benzyl-2-methyl-4-nitroaniline Crystals,” *Jpn. J. Appl. Phys.* **45**(5R), 4068 (2006).

<sup>36</sup> U. Puc, T. Bach, P. Günter, M. Zgonik, and M. Jazbinsek, “Ultra-Broadband and High-Dynamic-Range THz Time-Domain Spectroscopy System Based on Organic Crystal Emitter and Detector in Transmission and Reflection Geometry,” *Advanced Photonics Research* **2**(4), 2000098 (2021).

<sup>37</sup> S. Mansourzadeh, T. Vogel, A. Omar, M.F. Biggs, E.S.-H. Ho, C. Hoberg, D.J. Michaelis, M. Havenith, J.A. Johnson, and C.J. Saraceno, “High-dynamic-range broadband terahertz time-domain spectrometer based on organic crystal MNA,” *Photon. Res., PRJ* **13**(9), 2510–2519 (2025).

<sup>38</sup> A.-L. Viotti, M. Seidel, E. Escoto, S. Rajhans, W.P. Leemans, I. Hartl, and C.M. Heyl, “Multi-pass cells for post-compression of ultrashort laser pulses,” *Optica* **9**(2), 197–216 (2022).

<sup>39</sup> G. Andriukaitis, D. Kartashov, D. Lorenc, A. Pugžlys, A. Baltuška, L. Giniūnas, R. Danielius, J. Limpert, T. Clausnitzer, E.-B. Kley, A. Voronin, and A. Zheltikov, “Hollow-fiber compression of 6 mJ pulses from a continuous-wave diode-pumped single-stage Yb,Na:CaF<sub>2</sub> chirped pulse amplifier,” *Opt. Lett.* **36**(10), 1914 (2011).

<sup>40</sup> P.S.J. Russell, P. Hölzer, W. Chang, A. Abdolvand, and J.C. Travers, “Hollow-core photonic crystal fibres for gas-based nonlinear optics,” *Nature Photon* **8**(4), 278–286 (2014).

<sup>41</sup> K. Wang, Z. Zheng, H. Li, X. Meng, Y. Liu, Y. Tian, and L. Song, “Efficient strong-field THz generation from DSTMS crystal pumped by 1030 nm Yb-laser,” *Applied Physics Letters* **124**(12), 121102 (2024).

<sup>42</sup> W. Cui, A.W. Schiff-Kearn, E. Zhang, N. Couture, F. Tani, D. Novoa, P.St.J. Russell, and J.-M. Ménard, “Broadband and tunable time-resolved THz system using argon-filled hollow-core photonic crystal fiber,” *APL Photonics* **3**(11), 111301 (2018).

<sup>43</sup> A. Halpin, N. Couture, and J.-M. Ménard, “Optical pulse structuring in gas-filled hollow-core kagomé PCF for generation and detection of phase-locked multi-THz pulses [Invited],” *Opt. Mater. Express* **9**(7), 3115 (2019).

<sup>44</sup> A.D. Pryamikov, A.S. Birukov, A.F. Kosolapov, V.G. Plotnichenko, S.L. Semjonov, and E.M. Dianov, “Demonstration of a waveguide regime for a silica hollow - core microstructured optical fiber with a negative curvature of the core boundary in the spectral region > 3.5 μm,” *Opt. Express*, **OE** **19**(2), 1441–1448 (2011).

<sup>45</sup> M. Cassataro, D. Novoa, M.C. Günendi, N.N. Edavalath, M.H. Frosz, J.C. Travers, and P.S.J. Russell, “Generation of broadband mid-IR and UV light in gas-filled single-ring hollow-core PCF,” *Opt. Express*, **OE** **25**(7), 7637–7644 (2017).

<sup>46</sup> T.-C. Truong, D. Khatri, C. Lantigua, C. Kincaid, and M. Chini, “Few-cycle Yb-doped laser sources for attosecond science and strong-field physics,” *APL Photonics* **10**(4), 040902 (2025).

<sup>47</sup> J. Huang, N. Xu, Y. Wu, X. Ran, Y. Fang, H. Zhu, W. Wang, H. Chen, and S. Deng, “Interactions of Terahertz Photons with Phonons of Two-Dimensional van der Waals MoS<sub>2</sub>/WSe<sub>2</sub>/MoS<sub>2</sub> Heterostructures and Thermal Responses,” *Materials* **18**(7), 1665 (2025).

<sup>48</sup> G. Carini, R. Niemann, N.S. Mueller, M. Wolf, and A. Paarmann, “Surface Phonon Polariton Ellipsometry,” *ACS Photonics* **12**(2), 792–800 (2025).

<sup>49</sup> Y. Fang, J. Hao, J. Sang, J. Gao, L. Song, Y. Tian, and R. Li, “Coherent manipulation of second-harmonic generation via terahertz-field mediated phonon-polariton in zinc oxide,” *Nat Commun* **16**(1), 5598 (2025).

<sup>50</sup> R. Xu, T. Lin, J. Luo, X. Chen, E.R. Blackert, A.R. Moon, K.M. JeBailey, and H. Zhu, “Phonon Polaritonics in Broad Terahertz Frequency Range with Quantum Paraelectric SrTiO<sub>3</sub>,” *Advanced Materials* **35**(32), 2302974 (2023).

<sup>51</sup> J.C. Travers, “Optical solitons in hollow-core fibres,” *Optics Communications* **555**, 130191 (2024).

<sup>52</sup> T. Yasui, E. Saneyoshi, and T. Araki, “Asynchronous optical sampling terahertz time-domain spectroscopy for ultrahigh spectral resolution and rapid data acquisition,” *Appl. Phys. Lett.* **87**(6), 061101 (2005).

<sup>53</sup> T. Furuya, E.S. Estacio, K. Horita, C.T. Que, K. Yamamoto, F. Miyamaru, S. Nishizawa, and M. Tani, “Fast-Scan Terahertz Time Domain Spectrometer Based on Laser Repetition Frequency Modulation,” *Jpn. J. Appl. Phys.* **52**(2R), 022401 (2013).

<sup>54</sup> C. Hoberg, P. Balzerowski, and M. Haverinith, “Integration of a rapid scanning technique into THz time-domain spectrometers for nonlinear THz spectroscopy measurements,” *AIP Advances* **9**(3), 035348 (2019).

<sup>55</sup> W. Cui, K.M. Awan, R. Huber, K. Dolgaleva, and J.-M. Ménard, “Broadband and High-Sensitivity Time-Resolved THz System Using Grating-Assisted Tilted-Pulse-Front Phase Matching,” *Advanced Optical Materials* **10**(1), 2101136 (2022).

<sup>56</sup> W. Cui, E.K. Yalavarthi, A.V. Radhan, M. Bashirpour, A. Gamouras, and J.-M. Ménard, “High-field THz source centered at 2.6 THz,” *Opt. Express*, *OE* **31**(20), 32468–32477 (2023).

<sup>57</sup> I.C. Tangen, G.A. Valdivia-Berroeta, L.K. Heki, Z.B. Zaccardi, E.W. Jackson, C.B. Bahr, (Enoch) Sin-Hang Ho, D.J. Michaelis, and J.A. Johnson, “Comprehensive characterization of terahertz generation with the organic crystal BNA,” *J. Opt. Soc. Am. B, JOSAB* **38**(9), 2780–2785 (2021).